nature communications

Article

https://doi.org/10.1038/s41467-023-39541-y

Designing main-group catalysts for low-temperature methane combustion by ozone

Received: 24 August 2022

Accepted: 16 June 2023

Published online: 03 July 2023

Check for updates

Shunsaku Yasumura[1], Kenichiro Saita[2], Takumi Miyakage[1], Ken Nagai[1], Kenichi Kon[1], Takashi Toyao[1], Zen Maeno[3], Tetsuya Taketsugu[2,4] & Ken-ichi Shimizu[1]

The catalytic combustion of methane at a low temperature is becoming increasingly key to controlling unburned CH_4 emissions from natural gas vehicles and power plants, although the low activity of benchmark platinum-group-metal catalysts hinders its broad application. Based on automated reaction route mapping, we explore main-group elements catalysts containing Si and Al for low-temperature CH_4 combustion with ozone. Computational screening of the active site predicts that strong Brønsted acid sites are promising for methane combustion. We experimentally demonstrate that catalysts containing strong Bronsted acid sites exhibit improved CH_4 conversion at 250 °C, correlating with the theoretical predictions. The main-group catalyst (proton-type beta zeolite) delivered a reaction rate that is 442 times higher than that of a benchmark catalyst (5 wt% Pd-loaded Al_2O_3) at 190 °C and exhibits higher tolerance to steam and SO_2. Our strategy demonstrates the rational design of earth-abundant catalysts based on automated reaction route mapping.

The past decades have witnessed the widespread utilization of natural gas as a clean fuel for vehicles and power plants. The catalytic combustion of methane (CH_4) into carbon dioxide (CO_2) is becoming an increasingly valuable strategy for addressing the emissions of unburned CH_4, which exerts a greenhouse gas effect that is 22 times higher than that of CO_2[1–3]. Different types of heterogeneous catalysts, such as platinum-group-metal (PGM-)[4–7] and metal-oxide-based catalysts[8–10], have been reported. Among them, PGM-based catalysts, such as Pd- and Pt-loaded Al_2O_3, exhibited the highest catalytic activities[11]. However, the Pd-based catalysts suffer from high operating temperatures (>500 °C) under humidity conditions, as well as irreversible deactivation by sulfation during the co-feeding of steam and SO_2[2,12–14]. Moreover, large amounts of PGMs (200–266 g) must be utilized to achieve the combustion of CH_4 in a natural-gas-fueled heavy-duty vehicle[15]. Additionally, the mining and purification of PGMs extensively impact the environment (the productions of 1 kg each of Pt and Pd generate 12,500 and 3880 kg of CO_2 equivalents, respectively). Conversely, the production of main-group elements generates significantly lower CO_2 equivalents (e.g., 8.2 kg of Al)[16,17]. Thus, it is highly desirable (economically and ecologically) to develop main-group catalysts that can function at <200 °C in the co-presence of steam and SO_2.

Conventional catalyst screening, which is based on trial-and-error experiments, may not yield discontinuous discoveries, such as the main-group-facilitated catalytic combustion of CH_4 at low temperatures. The computational reaction route mapping of the unexplored chemical reaction space can benefit the discovery of different catalytic reactions[18–23]. Generally, the computations of the elementary steps in combustion reactions are considered challenging because of the abundant intermediates and products that exhibit similar formation energies and activation barriers (*Ea*)[24]. To comprehensively explore the various reaction routes, density functional theory (DFT)-based automated methods for predicting reaction pathways are promising because they link the theoretical prediction to the practical designs of

[1]Institute for Catalysis, Hokkaido University, N-21 W-10, Sapporo, Hokkaido 001-0021, Japan. [2]Department of Chemistry, Faculty of Science, Hokkaido University, Sapporo, Hokkaido 060-0810, Japan. [3]School of Advanced Engineering, Kogakuin University, Tokyo 192-0015, Japan. [4]Institute for Chemical Reaction Design and Discovery (WPI-ICReDD), Hokkaido University, Sapporo, Hokkaido 001-0021, Japan. e-mail: kshimizu@cat.hokudai.ac.jp

catalysts[25–30]. Maeda et al. developed an efficient automated path-searching method, namely the artificial force-induced reaction (AFIR) method, which involves pressing the atoms in given reactant molecules together by applying artificial force to form new structures (products) and assigning their transition states (TS)[30–41]. Via AFIR, they elucidated the entire reaction pathways of uncatalyzed reactions[32,37,39,40]. The automated reaction route mapping of heterogeneous catalysis systems is still formidable owing to the complexity of the surface reactions on solid materials, where the adsorption/desorption of the reactants and products, diffusion/migration of the adsorbates, and bond rearrangements proceed simultaneously[35,36,41].

Ozone (O_3), a strong oxidant[42], is generated onsite by a commercial ozonizer. O_3 has been employed to enhance the catalytic performance of the gas-phase combustion of volatile organic compounds, including toluene[43–45], acetone[46,47], and benzene[48,49]. Regarding the combustion of CH_4 with O_3[50–52], zeolite-based catalysts, such as Pd[53]–, Fe[54]–, Co[55]–, and proton[56]-type zeolites, have demonstrated efficiencies at low temperatures. However, the reported studies only considered the catalytic performance; thus, the strategy for designing the catalysts based on the detailed mechanism and elementary steps must still need to be addressed.

Herein, based on a computational design concept employing the AFIR method, we report a main-group catalyst for driving catalytic combustion of CH_4 with O_3 at low temperatures. First, we explored the $CH_4 + O_3$ reaction network toward generating CO_2 (Fig. 1a), confirming that the formation of methanol (CH_3OH), $CH_4 + O_3 \rightarrow CH_3OH + O_2$, was the rate-determining step (RDS) of CH_4 combustion. Thereafter, we performed the virtual screening of the active sites for RDS to propose the following concept: stronger Brønsted acid sites (BASs) exhibit higher catalytic activities (Fig. 1b). This concept was experimentally verified via CH_4 combustion tests employing O_3 at 250 °C in the presence of different BAS catalysts exhibiting different acid strengths (Fig. 1c). Finally, we demonstrated that a proton-type beta zeolite with Si/Al = 8.5 (Hß8.5) exhibited a reaction rate that was three orders of magnitude higher than that of a PGM-based benchmark catalyst, 5 wt% Pd-loaded Al_2O_3 ($Pd5Al_2O_3$). The developed catalyst exhibited very high resistance to steam and SO_2 poisoning during the 170-h reaction test.

Results

Computation of the reaction pathways toward CH_4 combustion by O_3

We explored the reaction pathway of CH_4 and O_3 ($CH_4 + O_3$) via SC-AFIR, which was an automated method for searching for reaction paths, as implemented in the GRRM program. Employing this method, the reaction routes of the non-catalytic oxidation of CH_4 into CO_2 by O_3 are automatically mapped. Figure 2a shows the reaction pathways with the corresponding values of their relative energies (ΔE) and *Ea*. In the first reaction, CH_4 is oxidized by O_3 to yield CH_3OH and O_2 with strong exothermicity (243.0 kJ/mol). In the TS structure, one O atom of O_3 extracts one H atom of CH_4 to yield CH_3 and OOOH fragments, where the evaluated E_a is 142.7 kJ/mol. This value is comparable to the reported experimental value for gas-phase CH_4 combustion by O_3 (148 kJ/mol)[57]. Next, the reactivity of CH_3OH with O_3 is assessed by exploring the reaction pathway via the SC-AFIR method (see Supplementary Fig. S1). Although CH_3OH is oxidized into formaldehyde (CH_2O), H_2O, and O_2 by O_3, $CH_3OH + O_3 \rightarrow CH_2O + H_2O + O_2$, via an exothermic reaction (210.1 kJ/mol), the process requires a very high E_a (255.1 kJ/mol). Alternatively, the oxidation of CH_3OH by O_2 produces CH_2O and H_2O_2, $CH_3OH + O_2 \rightarrow CH_2O + H_2O_2$, via a low E_a of 76.1 kJ/mol (Fig. 2a). The subsequent oxidation of CH_2O by H_2O_2 yields formic acid (CH_2O_2) and H_2O, $CH_2O + H_2O_2 \rightarrow CH_2O_2 + H_2O$, with an E_a of 124.2 kJ/mol. The decomposition of the produced CH_2O_2 yields CO_2 and H_2, $CH_2O_2 \rightarrow CO_2 + H_2$, or CO and H_2O molecules, $CH_2O_2 \rightarrow CO + H_2O$. However, these decomposition processes require high E_a to produce CO_2 and CO (264.3 and 296.3 kJ/mol, respectively) because of the high stability of CH_2O_2. As an alternative reaction path, we explored the oxidation of CH_2O by O_2, which was abundantly present in the practical systems, via SC-AFIR (see Supplementary Fig. S2). Thus, the oxidation of CH_2O by O_2 represents a facile process for producing CO and H_2O_2 via an E_a of 113.7 kJ/mol. The CO was oxidized into $CO_2 + O_2$ by O_3 through an E_a of 84.9 kJ/mol (see Supplementary Fig. S3). For comparison, Nitrous oxide (N_2O) and H_2O_2 were assessed as alternative oxidants to oxidize CH_4 into CH_3OH (see Supplementary Fig. S4). The evaluated E_a of the $CH_4 + N_2O$ and $CH_4 + H_2O_2$ reactions are 269 and 177 kJ/mol, respectively, indicating that O_3 is the most efficient oxidant for producing CH_3OH.

Employing the explored reaction pathways (Fig. 2b), the reaction, $CH_4 + O_3 \rightarrow CH_3OH + O_2$, was determined as the crucial process, with the highest E_a in the CH_4 oxidation reaction (the RDS). To further elucidate the TS structure of this reaction, Bader charge analysis was performed to investigate the distribution of charge on each atom in the TS structure (Fig. 2b). The total atomic charges in the CH_3 fragment are almost neutral (+0.12), indicating that it is a radical-like fragment. Regarding the OOOH fragment, the structure is divided into two parts: (I) the part comprising the H and O atoms that are closer to the CH_3 fragment (denoted as O1) and (II) that comprising the other two O atoms (denoted as O2 and O3). In the former part, the determined atomic charges of the H and O1 atoms are +0.56 and −0.58, respectively, while those of the O2 and O3 atoms in the

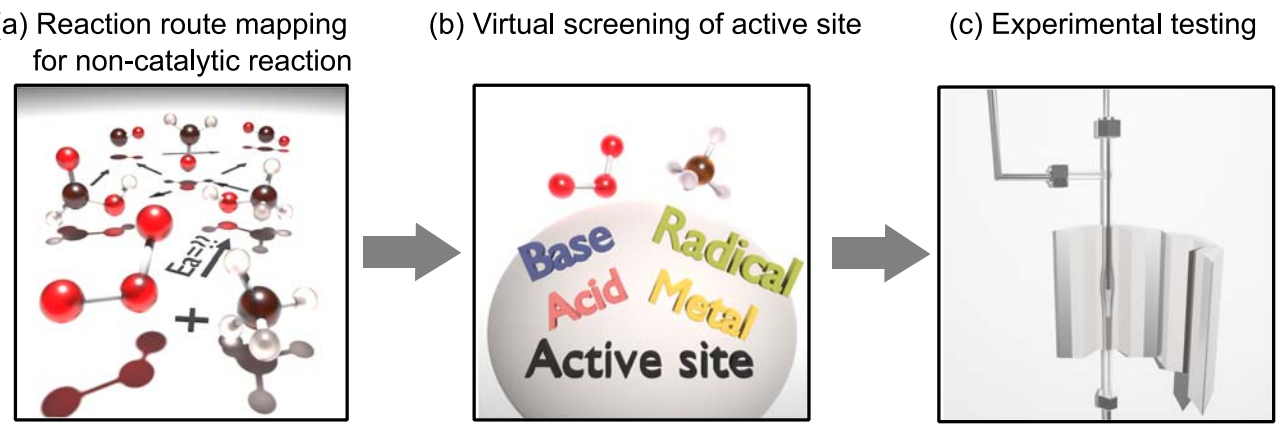

Fig. 1 | Rational design concept for catalytic combustion of CH_4 with O_3. **a** Employing single-component (SC)-AFIR, CH_4 combustion with O_3 was comprehensively explored to determine the key intermediates and elementary steps. **b** Different active sites were evaluated regarding the decrease in E_a of the key elementary step. **c** Heterogeneous catalyst comprising the predicted active site was tested experimentally.

https://doi.org/10.1038/s41467-023-39541-y

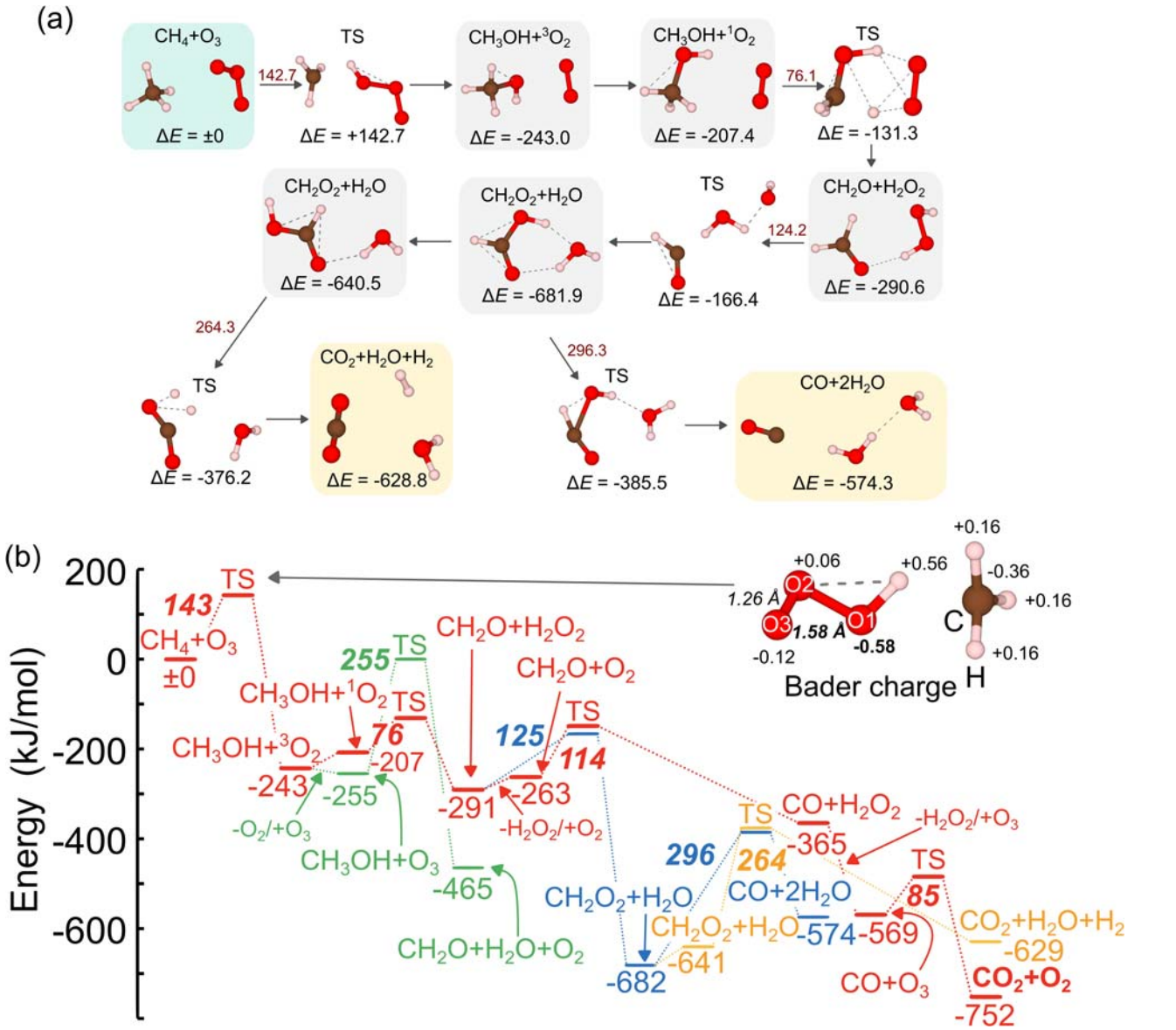

Fig. 2 | Result of reaction route mapping for $CH_4 + O_3$ reaction without active sites. a Calculated reaction pathway of $CH_4 + O_3$, as well as the values of relative energies (ΔEs). The values written in dark red represent E_a. **b** Energy profile of CH_4 combustion to yield CO_2. The reaction path shown by the red lines is the most plausible for CO_2 formation. The result of the Bader charge analyses of the TS structures of $CH_4 + O_3$ and $CH_3OH + O_3$ is shown together. ΔEs are provided under each bar, and the E_a are described employing the bold italic style (Unit: kJ/mol).

latter part are +0.06 and −0.12, respectively. This charge distribution indicates that the OOOH fragment comprises a OH radical and O_2 molecular species.

Virtual screening of catalytic sites for the reaction of $CH_4 + O_3$ to produce $CH_3OH + O_2$

The oxidation of CH_4 by O_3 into CH_3OH and O_2 was determined as the key reaction during CH_4 combustion (Computation of the reaction pathways toward CH4 combustion by O_3). To conduct the virtual screening of the catalytically active sites that effectively decrease the *Ea*, we carried out SC-AFIR calculations for the $CH_4 + O_3$ reaction on the following model active sites: (a) a Cu(0) atom as a redox site, (b) an NO molecule as a radical species, (c) pyridine (C_5H_5N) as a Brønsted and Lewis base site, and (d) sulfuric acid (H_2SO_4) as a Brønsted acid site (Fig. 3). Lewis acid site is not considered here because it is known that Lewis acid sites are rapidly deactivated in the presence of H_2O and SO_2, which are abundantly contained in the exhaust gases and produced by the CH_4 combustion reaction. Figure 3a shows the reaction path of $CH_4 + O_3$ over Cu(0). First, the C–H bond of CH_4 is cleaved by the O atom of O_3 over the Cu atom to yield OH and CH_3 groups on the Cu(II) cation ($Cu(OH)(CH_3)$), as well as adsorbed O_2 molecules through a high E_a (318.2 kJ/mol). Subsequently, the adsorbed O_2 molecule interacts with the neighboring CH_3 group to form CH_3OO species on the Cu(II) cation ($Cu(OH)(CH_3OO)$) via an E_a of 115.4 kJ/mol, while the extraction of the H atom of the OH group ($Cu(O)(OOH)(CH_3)$) is determined as an unfavorable path. Finally, the $Cu(OH)_2$ species and CH_2O are produced with a moderate barrier (108.7 kJ), although the Cu(II) cation was not reduced back into the Cu(0) atom. The maximum barrier was higher than that of the uncatalyzed reaction (142.7 kJ/mol). Hence, the Cu(0) atom was not a suitable catalyst for the $CH_4 + O_3$ reaction. Further, the NO molecules as a representative radical site reacted with O_3 to yield O_2 and NO_2, where the H atom of CH_4 was subsequently extracted to yield the CH_3 radical species that were bound to the nitrous acid (HONO) species (Fig. 3b). Although the evaluated E_a of this step was relatively low (122.7 kJ/mol), that of the reverse reaction ($CH_3\bullet$ + HONO → $CH_4 + NO_2$) was very

https://doi.org/10.1038/s41467-023-39541-y

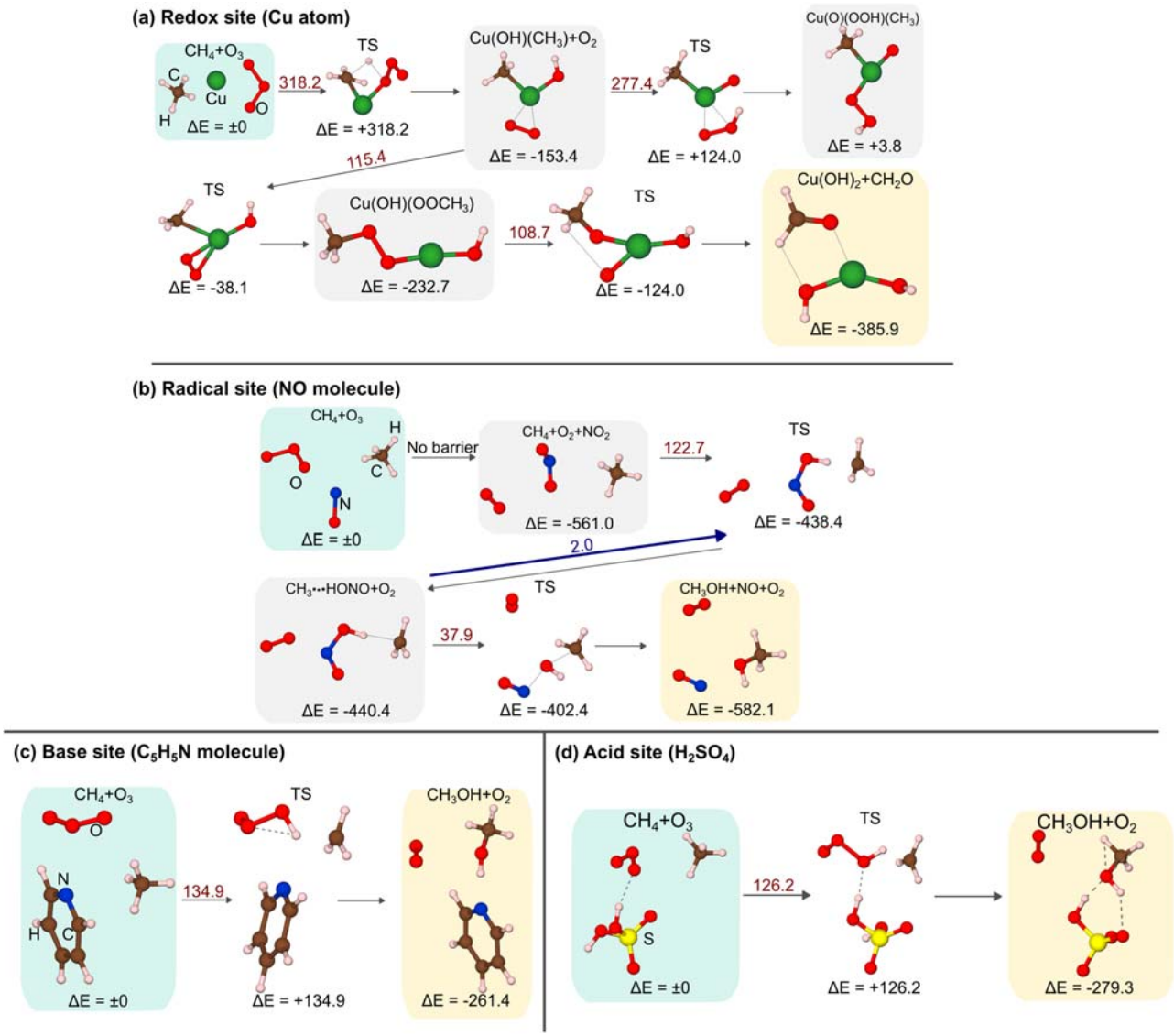

Fig. 3 | Result of reaction route mapping for $CH_4 + O_3$ reaction on model active sites. Calculated reaction pathways of $CH_4 + O_3$ on **a** Cu(0) atom, **b** NO molecule, **c** C_5H_5N molecule, and **d** H_2SO_4 molecule. The values of ΔE and the E_a (dark red) are shown together (Unit: kJ/mol).

low (2.0 kJ/mol). Additionally, the reaction, $NO_2 + CH_4$, to yield $CH_3OH + O_2$ shows only a low exothermicity (−21.1 kJ/mol). These results indicate that NO is also an inefficient catalyst for the $CH_4 + O_3$ reaction. To compare the result above with more realistic models, the reaction route mappings on the Cu metal cluster and FeO species in ZSM-5 zeolite were carried out only for the first step of CH_4 activation (supplementally Fig. S5). Note that the CH_4 activation on FeO species in ZSM-5 zeolite is known to proceed via the formation of CH_3 radical, similar to the case of the NO molecule in Fig. 3b[58]. The results indicate that, although E_a for CH_4 are different, the tendency of each active site is similar (high E_a of reducing back and low E_a of reverse-reaction for metal and radical sites, respectively). In the case of C_5H_5N as a base site, O_3 slightly interacted with the basic site (the N atom) of C_5H_5N before reacting with CH_4; thus, O_3 was not decomposed by the active site (Fig. 3c). Thereafter, CH_3OH was produced through a similar TS structure to the gas-phase one, and the product, which was weakly bound to the base site, was slightly more stable than that in the gas phase ($\Delta E = -264$ kJ (on the base site) vs −243 kJ (in the gas phase)), while their E_a were comparable ($E_a = 134.9$ vs 142.7 kJ/mol). Finally, H_2SO_4 was assessed as an acid site. CH_3OH was produced via an E_a of 126.2 kJ/mol, which was lower than that of the gas-phase reaction (142.7 kJ/mol), with very high exothermicity ($\Delta E = -279.3$ kJ/mol; Fig. 3d). As representative PGMs, Pd atom was also assessed as a potential active site for $CH_4 + O_3$ reaction (Supplementary Fig. S6). The result shows that the highest activation barrier in the reaction coordinates toward CH_2O is 109.3 kJ/mol. Since Pd-based catalysts are known to be efficient catalysts for CH_4 combustion by O_2, our result agrees with the previous reports[3,53,57,59]. Thus, the activity of Pd-based catalysts (Pd-loaded Al_2O_3 and Pd-exchanged zeolite) for $CH_4 + O_3$ reaction will be experimentally tested later. Consequently, we predicted that BASs were the most effective among the virtually screened active sites for $CH_4 + O_3$. In the next section, we discussed the preferable property of BAS, as well as the detailed mechanism of decreasing E_a.

Promotion effect of BAS on the $CH_4 + O_3$ reaction

We investigated the effect of the acid strength of BASs of the mineral acids on the E_a of $CH_4 + O_3$. H_2SO_4, perchloric acid ($HClO_4$), nitric acid (HNO_3), and phosphoric acid (H_3PO_4) were evaluated as BASs exhibiting different acidities. The initial structure (IS), final structure (FS), and TS are shown in Supplementary Fig. S7. The E_a of the strong acids (128.4 and 126.2 kJ/mol for $HClO_4$ and H_2SO_4, respectively) are lower

https://doi.org/10.1038/s41467-023-39541-y

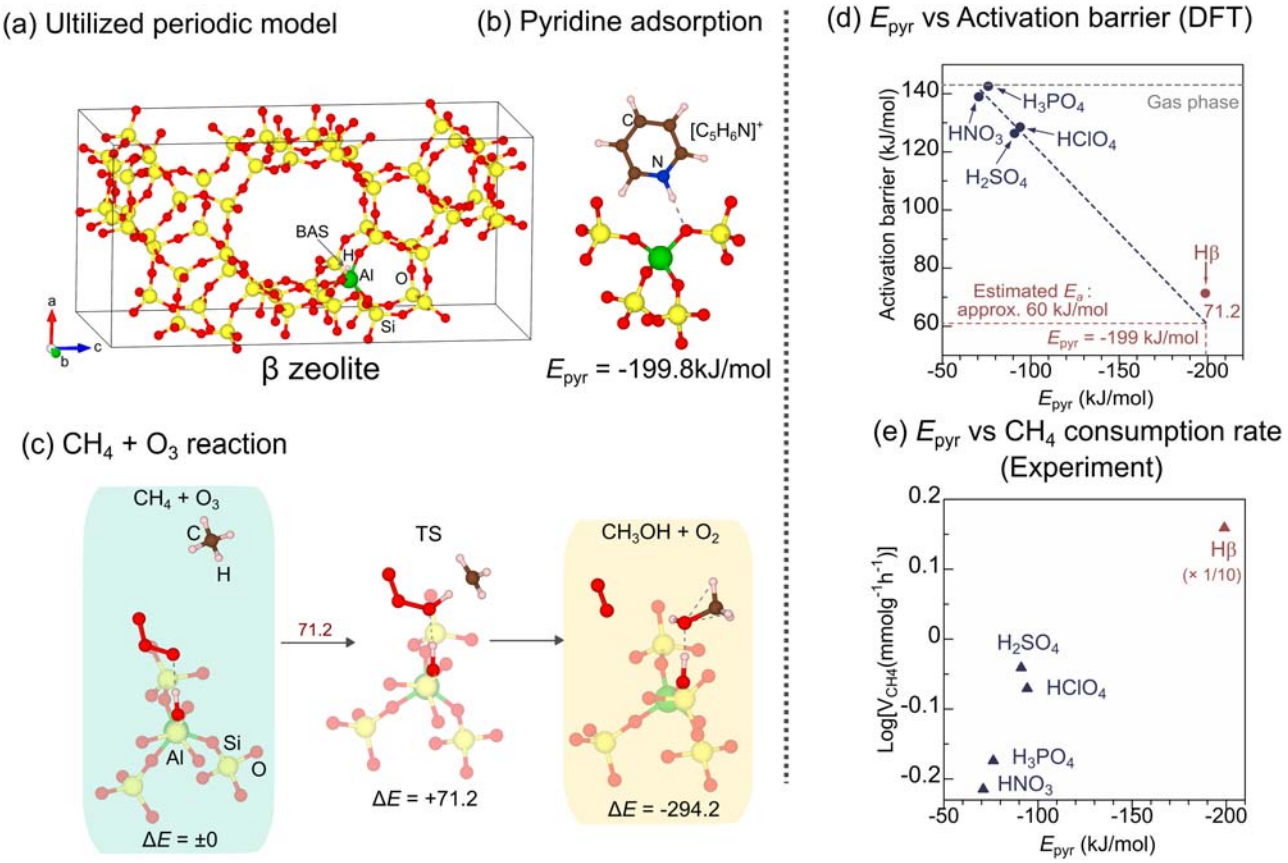

Fig. 4 | Theoretical and experimental evaluation for the effect of acid sites on $CH_4 + O_3$ reaction. a Employed periodic model of the ß zeolite. **b** Structure of the adsorption of C_5H_5N on BAS of ß zeolite. **c** TS calculations of the $CH_4 + O_3$ reaction on BAS of the ß zeolite. ΔE is reported in the kJ/mol unit. E_a is shown in dark red. **d** Plot of E_a of the $CH_4 + O_3$ reaction as a function of the C_5H_5N-stabilization energy (E_{pyr}) of the acids. **e** CH_4 consumption rate of the samples in 0.1% CH_4 + 0.7% O_3 at 250 °C (He balance, total flow: 100 ml/min) as a function of E_{pyr}.

than that of the uncatalyzed reaction (142.7 kJ/mol), which is close to the value for a weak acid (142.2 and 138.8 kJ/mol for H_3PO_4 and HNO_3, respectively).

To quantitatively evaluate the impact of the acid property, the E_a of the $CH_4 + O_3$ reaction are plotted as a function of the stabilization energy of C_5H_5N on BASs (E_{pyr}), as determined by DFT calculations. Notably, the adsorption of C_5H_5N on BAS of solid material has been widely applied to experimentally and theoretically analyze its acidity[60–62]. The values of E_{pyr} for $HClO_4$, H_2SO_4, HNO_3, and H_3PO_4 are −94.3, −91.1, −70.9, and −76.2 kJ/mol, respectively. This result corresponds to their experimentally obtained deprotonation enthalpies (see Supplementary Table S1). Figure 4d shows that the E_a of the $CH_4 + O_3$ reaction on BASs decreased with the increasing acid strengths, indicating that relatively strong BASs correspond to higher reaction rates for the $CH_4 + O_3$ reaction. To understand the activation mechanism within the frontier orbital theory, the projected crystal orbital Hamilton population (pCOHP) of an isolated O_3 molecule was analyzed and described in Fig. 5a. There are two anti-bonding orbitals around the Fermi level (E_F) in the pCOHP curve of O–O bond. In the visualization of their orbitals, lower and higher energies show π* and σ* characters, respectively. Since they have anti-bonding character, it is expected that more electron charge transfer to them induces weakening of the O–O bond. Figure 5b, c shows the Bader charge of O1 atom and the bond length of O1–O2 bond, respectively, against E_{pyr} in TS structure of $CH_4 + O_3$ reaction (the representative TS structure is shown in Fig. 5d and others are shown in supplementary Fig. S8). By increasing E_{pyr}, the charge of O1 atom increases while O1–O2 bond is elongated, indicating that the O_3 molecule was more activated on the acids with higher E_{pyr}. A schematic description of the activation scheme is shown in Fig. 5e. By the electrostatic interaction between BAS and O1 atom, the charge transfer to O1 atom occurs, resulting in the elongation of O1–O2 bond, and thus, the BASs with high E_{pyr} efficiently decrease the E_a of $CH_4 + O_3$ reaction.

Inspired by the gained insight into BASs as active sites, a proton-type zeolite (ß-type) was theoretically examined for the adsorption of C_5H_5N (Fig. 4a, b). The result indicates the higher E_{pyr} of the zeolite (E_{pyr} = −199.8 kJ/mol) than that of H_2SO_4 (−91.1 kJ/mol). Note that E_{pyr} reflects not only the strength of acidity but also the confinement effect of the zeolite cage that also probably affects the CH_4 combustion reaction[63,64]. The extrapolation of the linear relationship between E_{pyr} and E_a of the mineral acids indicates that the zeolite might achieve an extremely low E_a (~60 kJ/mol). To verify this hypothesis, we conducted TS calculations for the $CH_4 + O_3$ reaction on the BAS of the zeolite. Figure 4c shows the optimized structures of IS, TS, and FS. As expected from the strong acidity of the zeolite, the computed E_a (71.2 kJ/mol) is considerably lower than those for the mineral acids (126.2–142.2 kJ/mol).

Next, we experimentally verified the theoretically predicted relationship between the E_a and E_{pyr} of the $CH_4 + O_3$ reaction. The mineral acid (3 wt% H_2SO_4, $HClO_4$, HNO_3, or H_3PO_4) was loaded onto an SiO_2 support and tested for the reaction in a 0.1% CH_4 + 0.7% O_3 flow (total flow: 100 ml/min, He balance) at 250 °C employing a fixed-bed flow reactor (the volatility of the acid was examined by H_2O on-off switching test; Fig. S10). The concentrations of CH_4 and O_3 in the outlet gas were monitored by a gas cell that was equipped with an infrared spectroscope (Supplementary Fig. S9 shows the illustration of the experimental setup). Their CH_4 conversion was maintained for 30 min. The obtained CH_4 consumption rates are plotted as a function of E_{pyr}

https://doi.org/10.1038/s41467-023-39541-y

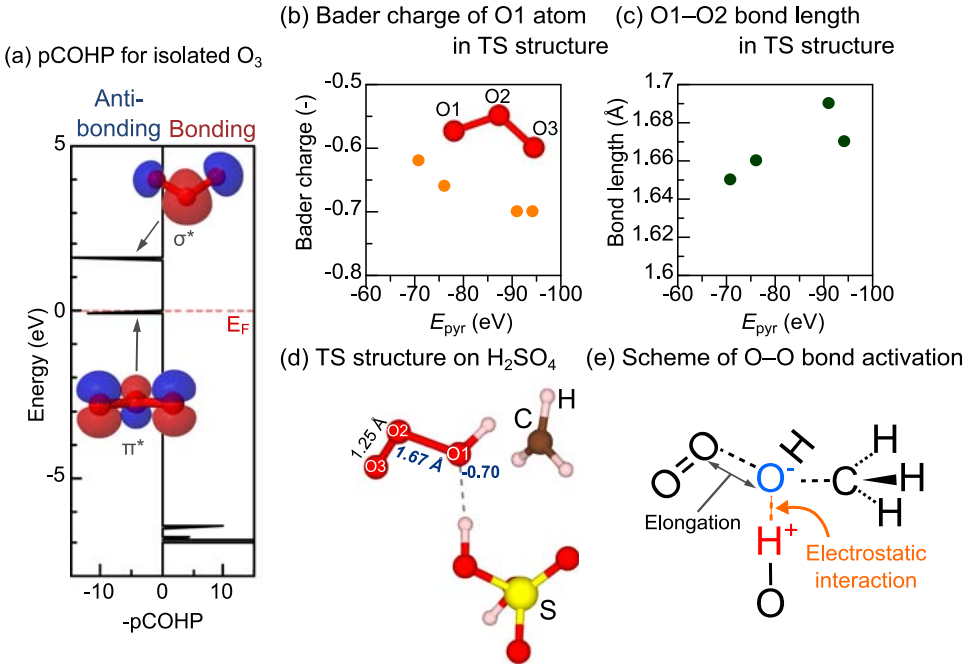

Fig. 5 | Theoretical interpretation of activation mechanism for $CH_4 + O_3$ reaction by acid sites. a The projected crystal orbital Hamilton population (pCOHP) curve for the O–O bond in the isolated O_3 molecule. **b** Bader charge of O1 atom and **c** O1–O2 bond length in TS structures against E_{pyr} (shown in supplementary Fig. S8). **d** TS structure of $CH_4 + O_3$ reaction over H_2SO_4 molecule. Bader charge of O1 atom and bond lengths are shown together. **e** The schematic description of O–O bond activation scheme.

(Fig. 4e). Interestingly, the observed consumption rates correlate moderately with E_{pyr}. Next, an Hß zeolite with a relatively low Si/Al ratio (8.5) (Hß8.5) was tested via the same reaction. Therein, Hß8.5 achieves an extremely higher consumption rate than H_2SO_4, demonstrating the highest rate among the tested catalysts. The above results demonstrate that the high CH_4-combustion activity of a strong BAS-based catalyst, Hß8.5, could be rationally predicted based on computational mapping of the reaction network, as well as TS calculations. In the next section (Performance of the Hß-catalyzed CH_4 combustion with O_3), we experimentally demonstrate the superior performance of Hß8.5 by comparing it with $Pd5Al_2O_3$ as a conventional catalyst.

Performance of the Hß-catalyzed CH_4 combustion with O_3

We conducted catalytic tests to experimentally demonstrate the catalytic performance of Hß8.5. Figure 6a shows the conversions of CH_4 over Hß8.5 and a benchmark catalyst ($Pd5Al_2O_3$) in a flow of 0.1% CH_4 + 5.95% O_2 + 0.7% O_3 at different temperatures. In 0.1% CH_4 + 10% O_2, Hß8.5 did not achieve CH_4 conversion in the entire temperature range, indicating the necessity of O_3 as the oxidant. In 0.1% CH_4 + 5.95% O_2 + 0.7% O_3, Hß8.5 achieved the high conversion of CH_4 at 200 °C, while $Pd5Al_2O_3$ required a temperature of >400 °C to achieve comparable performance. At >250 °C, the conversion of CH_4 over Hß8.5 decreased because O_3 conversion had reached 100% via self-decomposition (Fig. 5b). To evaluate the effect of Pd loading into zeolites, Pd-exchanged ß8.5 zeolite (Pdß8.5) was prepared and then tested, resulting in low CH_4 conversion in the low-temperature region due to full decomposition of O_3 similar to the result of $Pd5Al_2O_3$ (Supplementally Fig. S11). The effect of BAS on the self-decomposition of O_3 into O_2 ($2O_3 \rightarrow 3O_2$) was theoretically investigated because this reaction represented an obstacle to the practical application of O_3 as an oxidant. Supplementary Fig. S12 compares the optimized TS structures of the uncatalyzed and Hß-catalyzed decompositions of O_3. The calculated E_a of the uncatalyzed and Hß-catalyzed reactions are 42.3 and 69.5 kJ/mol, respectively, indicating that BAS in zeolite do not promote the self-decomposition of O_3. This property is desirable in catalysts for CH_4 combustion by O_3. Dissimilar to Hß8.5, $Pd5Al_2O_3$ exhibited high activity toward O_3 decomposition (complete conversion even at 50 °C); hence, the addition of O_3 did not increase the CH_4 combustion activity of $Pd5Al_2O_3$.

Figure 5c shows a plot of the conversions of CH_4 and O_3, as well as the BAS amounts, as evaluated by NH_3-adsorption measurement as a function of the Si/Al ratio of the utilized ß zeolites (Si/Al = 8.5, 12.5, 20, and 255). Evidently, the Al-rich ß zeolites with more BASs exhibited higher CH_4 conversions, which is consistent with the proposal from DFT calculation above. The Arrhenius plot of the Hß8.5-catalyzed CH_4 combustion with O_3 (Fig. 5d) revealed an apparent barrier (*Ea*) of 75 kJ/mol, which agrees with the theoretical value of the $CH_4 + O_3$ reaction to yield CH_3OH (E_a = 71.2 kJ/mol). The E_a of Hß8.5 was considerably lower than that of $Pd5Al_2O_3$ (E_a = 95 kJ/mol) in 0.1% CH_4 + 10% O_2. Supplementary Fig. S13 shows the results of the kinetic analyses for estimating the reaction orders. The reaction orders of CH_4 (0.2) and O_3 (0.2) were positive. Further, the reaction rates per weight of the catalyst (for Hß8.5 and $Pd5Al_2O_3$) for CH_4 conversion (V_{CH4}) at 190 °C were compared, and the result indicated that V_{CH4} of Hß8.5 (57.5 mmol h^{-1} g_{cat}^{-1}) was 442 times higher than that of $Pd5Al_2O_3$ (0.13 mmol h^{-1} g_{cat}^{-1}), demonstrating that the found main-group catalyst (Hß8.5) exhibited considerably higher activity toward CH_4 combustion than the PGM-based benchmark catalyst (scientific literature on the same reaction using proton-type zeolite are limited, and thus, it is difficult to compare with the previous reports.).

Further, Hß8.5 and $Pd5Al_2O_3$ were tested for CH_4 combustion in the co-presence of H_2O and SO_2 to compare their resistance to steam and SOx poisoning. Figure 5f shows the time course of CH_4 combustion over 40 mg of Hß8.5 (5.95% O_2 + 0.7% O_3 at 200 °C) and $Pd5Al_2O_3$ (10% O_2 at 400 °C) in 0.1% CH_4 + 3% H_2O + 40 ppm SO_2. By feeding H_2O and SO_2, the CH_4 conversion at 400 °C over $Pd5Al_2O_3$ decreased with the reaction time, reaching almost zero after 10 h. Conversely, the CH_4 conversion over Hß8.5 did not decrease at 200 °C even after 15 h, indicating that Hß8.5 was highly resistant to steam and SO_2 poisoning. Finally, 10 mg of Hß8.5 was examined for the long-term reaction test in

https://doi.org/10.1038/s41467-023-39541-y

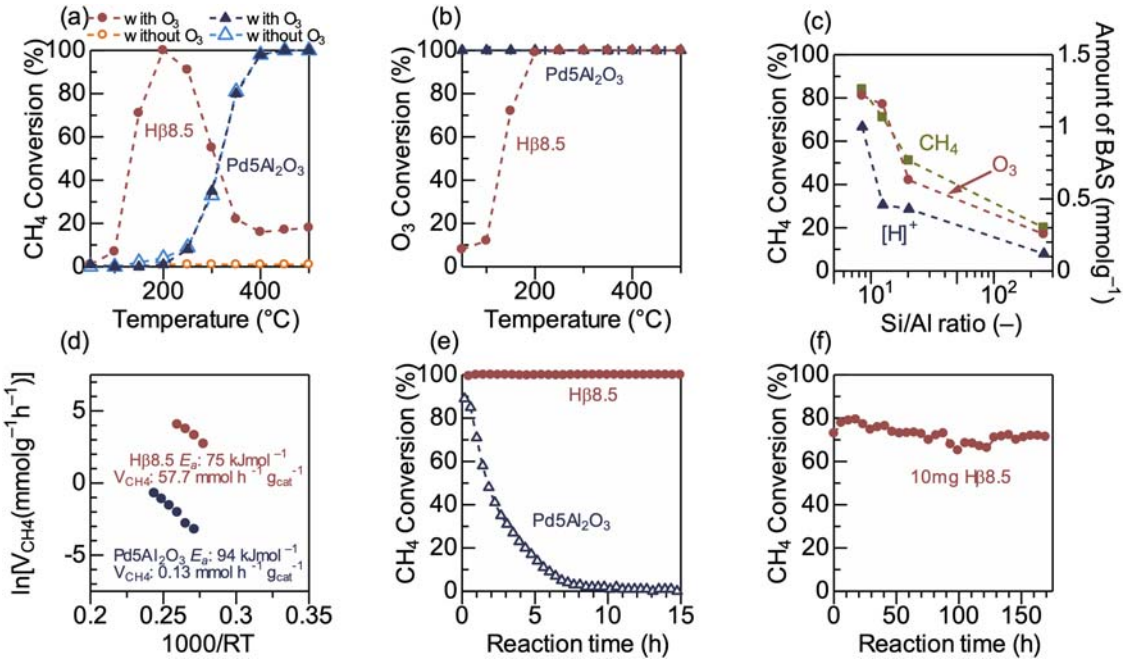

Fig. 6 | Catalytic test for CH_4 combustion reaction. a CH_4 and **b** O_3 conversions over 40 mg of the Hß zeolite with an Si/Al ratio of 8.5 (Hß8.5) and 40 mg of 5 wt% Pd-loaded Al_2O_3 ($Pd5Al_2O_3$) in 0.1% CH_4 + 5.95% O_2 + 0.7% O_3 and 0.1% CH_4 + 10% O_2 flows as functions of the reaction temperature. **c** Conversions of CH_4 and O_3 over 40 mg of the Hß zeolite with different Si/Al ratios (8.5, 12.5, 20, and 255) in a 0.1% CH_4 + 5.95% O_2 + 0.7% O_3 flow at 150 °C, together with the amount of BAS in the ß zeolite, as evaluated via NH_3-adsorption measurements. **d** Arrhenius plots for the combustions of CH_4 over Hß8.5 in 0.1% CH_4 + 5.95% O_2 + 0.7% O_3 at 160–190 °C, as well as over $Pd5Al_2O_3$ in 0.1% CH_4 + 10% O_2 at 170–220 °C. The reaction rates (V_{CH4}) at 190 °C over Hß8.5 and $Pd5Al_2O_3$ are shown together (R^2 = 0.99 for both catalyst). **e** Time course of CH_4 conversion over 40 mg of $Pd5Al_2O_3$ (at 400 °C) and Hß8.5 (at 200 °C) in 0.1% CH_4 + 3% H_2O + 40 ppm SO_2 + 10% O_2 or 5.95% O_2 + 0.7% O_3 for $Pd5Al_2O_3$ and Hß8.5, respectively, with He balance (total flow: 100 ml/min). **f** Long-term reaction test for 10 mg of Hß8.5 in 0.1% CH_4 + 5.95% O_2 + 0.7% O_3 + 3% H_2O + 40 ppm SO_2 at 200 °C.

0.1% CH_4 + 5.95% O_2 + 0.7% O_3 + 3% H_2O + 40 ppm SO_2 at 200 °C, and the result indicated that the catalyst did not significantly decrease the CH_4 conversion for 170 h of reaction time.

To investigate the mechanism of the catalytic CH_4 combustion by O_3 in the realistic condition, ab initio molecular dynamics (AIMD) was additionally carried out for CH_4 and O_3 separately. During the simulation, the O_3 molecule frequently interacted with BASs and was present near the sites. In contrast, the CH_4 molecule diffused throughout the zeolite cage and less frequently interacted with BASs. In fact, the calculated mean diffusion coefficient of the O_3 molecule is 5.0×10^{-4} Å^2/fs in the simulation, while that of the CH_4 molecule is 8.4×10^{-4} Å^2/fs. These results indicate that, in realistic conditions, the O_3 molecule is present near BASs, and once CH_4 reaches the sites, CH_4 and O_3 react to form CH_3OH and O_2.

Discussion

In this study, we rationally designed a catalyst for low-temperature O_3-driven catalytic combustion of CH_4 based on the elucidation of an unexplored reaction network. The $CH_4 + O_3$ reaction toward generating CO_2 was explored via SC-AFIR, and the formation of CH_3OH via $CH_4 + O_3$ ($CH_4 + O_3 \rightarrow CH_3OH + O_2$) was determined as RDS of CH_4 combustion (E_a = 142.7 kJ/mol). To assess the various types of active sites (acid, base, redox, and radical sites), model molecules (H_2SO_4, C_5H_5N, a Cu atom, and HNO_3) were introduced into the system, and reaction route was calculated. Among the examined active sites, H_2SO_4 effectively decreased the reaction (E_a = 126.2 kJ/mol); thus, different Brønsted acid catalysts with different acid strengths were examined for the TS calculation. The relationship between the acidity and calculated E_a of the $CH_4 + O_3$ reaction (CH_3OH formation) availed a facile catalyst design concept; the stronger the BASs afford the higher the catalytic activity. Thereafter, the theory-driven concept was experimentally verified by CH_4 combustion with O_3 at 250 °C. An Hß zeolite, which was the most effective candidate, as predicted by this concept, was experimentally tested for the $CH_4 + O_3$ reaction. The apparent activation energy (75 kJ/mol), which was estimated by the kinetic experiment, was consistent with the computed value (71.2 kJ/mol). Hß exhibited a very high reaction rate, which was 442 times higher than that of the benchmark catalyst, $Pd5Al_2O_3$, at 190 °C. During the catalytic tests in the presence of SO_2 and H_2O, Hß achieved the full conversion of CH_4 at 190 °C, whereas $Pd5Al_2O_3$ was completely deactivated even at a higher temperature (400 °C) owing to the poisoning of its active sites by water and SO_2. Finally, the developed catalyst (Hß zeolite) was tested in a 170-h long-term reaction that exhibited very high resistance against water and SO_2.

In summary, O_3, which was determined as an efficient oxidant, oxidized CH_4 into CH_3OH as the RDS. Among the considered active sites, BAS in H_2SO_4 molecule efficiently decreased the activation barrier of CH_3OH formation. After stronger BASs were evaluated to be promising theoretically and experimentally, proton-type zeolite, comprising strong BASs, was experimentally tested; Hß zeolite exhibited the superior CH_4 combustion rate in the presence of O_3. These results demonstrated that a computationally designed catalysis based on earth-abundant metal elements (Si and Al) and alternative oxidants could achieve higher activities and durabilities compared with their PGM-based ones for low-temperature CH_4 combustion.

Methods

DFT calculations

Spin-polarized DFT calculations were performed employing the generalized-gradient approximation of Perdew–Burke–Ernzerhof functional[65], as implemented in the Vienna Ab Initio Simulation Package[66,67] (VASP), and the projected augmented waves[68,69] method was employed for the Kohn–Sham equations with cut-off energy of 500 eV. The Γ point was employed for the Brillouin-zone sampling[70].

DFT-D3 dispersion correction with the Becke–Johnson damping was employed for all the calculations[71]. To simulate the gas-phase reaction, calculations were conducted within a large cubic cell ($a = b = c = 15$ Å). The structure of the β zeolite was obtained from the International Zeolite Association database[72], and the lattice constants were fixed at initial values ($a = b = 12.632$ Å, $c = 26.186$ Å, $\alpha = \beta = \gamma = 90.0°$) during the calculations. The SC-AFIR method, as implemented in the GRRM17 program[38], was applied for reaction route mapping with a model collision energy parameter of 1000 kJ/mol. Only a positive force was applied for the AFIR calculations. The H, O, and C atoms in the CH_4 and O_3 molecules were considered the targets of SC-AFIR. The locally updated plane method availed the path top points, which were subsequently optimized as TS structures and determined by the following intrinsic reaction coordinate calculation[73]. To calculate for the β zeolite, the atoms of the zeolitic framework, except for the Al atom, as well as the Si atoms adjacent to the Al and O atoms connecting to the adjacent Si, and H atoms of BAS were fixed at the crystallographic position (Fig. 4b). The stabilization energy of C_5H_5N was defined, as follows:

$$E_{pyr} = (E_{C5H5N\ on\ BAS} - E_{BAS} - E_{C5H5N}) \quad (1)$$

Thus, the total energies of the models including a C_5H_5N molecule, acid molecules, and C_5H_5N interacting with the acid molecules were described as E_{C5H5N}, E_{BAS}, and $E_{C5H5N\ on\ BAS}$, respectively. The pCOHP[74] was calculated by LOBSTER software[75]. The molecular orbitals were visualized with the VASPMO code[76]. The structures are visualized by VESTA software[77]. AIMD simulation was performed within the periodic-boundary condition as implemented in CP2K package[78]. The spin-unrestricted DFT calculation was carried out using the Perdew–Burke–Ernzerhof functional[65] within the generalized-gradient approximation. The valence electrons were described by the double-ζ valence plus polarization basis sets of the MOLOPT type[79], and the core electrons were represented by the Goedecker–Teter–Hutter pseudopotentials[80,81]. The energy cutoff was set to 500 Ry. Only the Γ-point was employed for the Brillouin zone integration. The Born–Oppenheimer MD simulation was carried out with the canonical (NVT) ensemble condition using the Nóse–Hoover thermostat to control the temperature. The time step was set to 1 fs. After equilibrating for 1 ps, 50 ps of the simulation was performed for each model comprising one CH_4 or O_3 molecule, respectively.

Catalysts preparations

1 g of proton-type (H) β zeolite with a Si/Al ratio of 8.5 (Hβ 8.5) was obtained via the calcination of an NH_4^+-type β zeolite that was purchased from Tosoh Co. (HSZ-920NHA) in the air at 500 °C. The 1 g of Hβ zeolites with Si/Al ratios of 20 and 255 (HSZ-940HOA and HSZ-980HOA, respectively) were supplied by Tosoh Co., and another with a Si/Al ratio of 12.5 was supplied by the Catalysis Society of Japan (JRC-Z-HB25). Note that the impurity of Hβ8.5 was checked by ICP measurement, and Fe, Co, Ni, Cu, and Zn were not detected (<0.01 wt%). Acid-load SiO_2 was prepared via impregnation method. 0.2 g of SiO_2 (CARiACT G–6, Fuji Silysia, S_{BET} = ca. 500 $m^2\ g^{-1}$) was suspended in an 0.5 M aqueous solution of H_2SO_4, $HClO_4$, H_3PO_4, and HNO_3 at room temperature. The water was evaporated at 50 °C from the mixture and dried in an oven at 90 °C. 1 g of Al_2O_3 was prepared by calcining γ-AlOOH (Catapal B Alumina, Sasol) for 3 h at 900 °C. Next, 1.05 g of 5 wt % Pd-loaded Al_2O_3 was prepared by impregnating 1 g of Al_2O_3 with an 0.005 M aqueous HNO_3 solution $Pd(NH_3)_2(NO_3)_2$. 0.5 g of Pd-exchanged ß zeolite (Pdß8.5) was prepared by exchanging NH_4^+–ß8.5 with an 0.005 M aqueous solution of $[Pd(NH_3)_4]Cl_2$ at room temperature for 20 h, followed by centrifuging and washing with deionized water, drying (100 °C, 20 h), and by calcining (500 °C, 1 h, in the air).

Catalytic test

The catalytic test was conducted under in 0.1% CH_4 + 0.7% O_3 + 5.95% O_2 (He balance, total flow:100 ml/min) as a typical condition. 40 mg of catalyst powder was set in the fixed-bed reactor using quartz wool and the outlet was directly connected to a JASCO FT/IR-4600 spectrometer that was equipped with a triglycine sulfate (TGS) detector, in which a homemade infrared (IR) gas cell, which was equipped with KBr windows, was placed to monitor the concentrations of CH_4 and O_3. For kinetic analysis, 5 mg of Hβ 8.5 was used to keep CH_4 conversion under 40%. The IR area of O_3 was calibrated employing an O_3 analyzer (EG-550, EcoDesign Inc.) to convert the area into concentration. To feed O_3 into the system, an O_2 flow was passed through an ozonizer (F0G-AC5G, EcoDesign Inc.) that was placed before the mainstream. The whole view of the employed setup is shown in Supplementary Fig. S9. The NH_3-adsorption measurement was carried out by Infrared spectroscopy (JASCO FT/IR-4200 spectrometer using a home-made in situ IR cell. The catalyst disc of the zeolite sample (40 mg,) was dehydrated under He flow at 500 °C before a background spectrum was recorded under a flow of He at 200 °C. Then, NH_3 (1%) flowed to the sample, followed by He purging before IR spectrum was taken at 200 °C.

Statistics and reproducibility

The experiments were not randomized.

Data availability

The source data, which support the result of this study, can be found in the manuscript and Supplementary information. Data are available from the corresponding author upon request.

Code availability

The VASP code package used in this work can be accessible after a user license is authorized by the VASP company (https://www.vasp.at). LOBSTER, VASPMO, VESTA, and CP2K codes can be freely accessible from the websites (LOBSTER: http://www.cohp.de, VASPMO: https://sourceforge.net/projects/vaspmo/, VESTA: https://jp-minerals.org/vesta/en/, and CP2K: https://www.cp2k.org). AIMD simulation was carried out using Quickstep module in CP2K code.

References

1. Petrov, A. W. et al. Stable complete methane oxidation over palladium based zeolite catalysts. *Nat. Commun.* **9**, 2545 (2018).
2. Petrov, A. W., Ferri, D., Tarik, M., Kröcher, O. & van Bokhoven, J. A. Deactivation aspects of methane oxidation catalysts based on palladium and ZSM-5. *Top. Catal.* **60**, 123–130 (2017).
3. Jiang, D., Khivantsev, K. & Wang, Y. Low-temperature methane oxidation for efficient emission control in natural gas vehicles: Pd and beyond. *ACS Catal.* **10**, 14304–14314 (2020).
4. Mahara, Y., Tojo, T., Murata, K., Ohyama, J. & Satsuma, A. Methane combustion over $Pd/CoAl_2O_4/Al_2O_3$ catalysts prepared by galvanic deposition. *RSC Adv.* **7**, 34530–34537 (2017).
5. Colussi, S., Fornasiero, P. & Trovarelli, A. Structure-activity relationship in Pd/CeO_2 methane oxidation catalysts. *Chin. J. Catal.* **41**, 938–950 (2020).
6. Xiong, H. et al. Engineering catalyst supports to stabilize PdO_x two-dimensional rafts for water-tolerant methane oxidation. *Nat. Catal.* **4**, 830–839 (2021).
7. Losch, P. et al. Modular Pd/zeolite composites demonstrating the key role of support hydrophobic/hydrophilic character in methane catalytic combustion. *ACS Catal.* **9**, 4742–4753 (2019).
8. Arai, H., Yamada, T., Eguchi, K. & Seiyama, T. Catalytic combustion of methane over various perovskite-type oxides. *Appl Catal.* **26**, 265–276 (1986).
9. Ferri, D. & Forni, L. Methane combustion on some perovskite-like mixed oxides. *Appl Catal. B* **16**, 119–126 (1998).

10. Tao, F. F. et al. Understanding complete oxidation of methane on spinel oxides at a molecular level. *Nat. Commun.* **6**, 7798 (2015).
11. He, L., Fan, Y., Bellettre, J., Yue, J. & Luo, L. A review on catalytic methane combustion at low temperatures: catalysts, mechanisms, reaction conditions and reactor designs. *Renew. Sustain. Energ. Rev.* **119**, 109589 (2020).
12. Goodman, E. D. et al. Catalyst deactivation via decomposition into single atoms and the role of metal loading. *Nat. Catal.* **2**, 748–755 (2019).
13. Yang, W. et al. A review on the impact of SO_2 on the oxidation of NO, hydrocarbons, and CO in diesel emission control catalysis. *ACS Catal.* **11**, 12446–12468 (2021).
14. Hou, Z. et al. Electronically engineering water resistance in methane combustion with an atomically dispersed tungsten on PdO catalyst. *Angew. Chem. Int. Ed.* **61**, e202201655 (2022).
15. Keenan, M. et al. The catalytic challenges of implementing a Euro VI heavy duty emissions control system for a dedicated lean operating natural gas engine. *Top. Catal.* **62**, 273–281 (2019).
16. Nuss, P. & Eckelman, M. J. Life cycle assessment of metals: a scientific synthesis. *PLoS One* **9**, 1–12 (2014).
17. Bullock, R. M. et al. Using nature's blueprint to expand catalysis with Earth-abundant metals. *Science* **369**, 2020 (*1979*).
18. Stocker, S., Csányi, G., Reuter, K. & Margraf, J. T. Machine learning in chemical reaction space. *Nat. Commun.* **11**, 1–11 (2020).
19. Kreitz, B. et al. Quantifying the impact of parametric uncertainty on automatic mechanism generation for CO_2 hydrogenation on Ni(111). *JACS Au* **1**, 1656–1673 (2021).
20. Lan, T. & An, Q. Discovering catalytic reaction networks using deep reinforcement learning from first-principles. *J. Am. Chem. Soc.* **143**, 16804–16812 (2021).
21. Nakao, A., Harabuchi, Y., Maeda, S. & Tsuda, K. Leveraging algorithmic search in quantum chemical reaction path finding. *Phys. Chem. Chem. Phys.* **24**, 10305–10310 (2022).
22. Xu, J., Cao, X. M. & Hu, P. Perspective on computational reaction prediction using machine learning methods in heterogeneous catalysis. *Phys. Chem. Chem. Phys.* **23**, 11155–11179 (2021).
23. Fu, X., Li, J., Long, J., Guo, C. & Xiao, J. Understanding the product selectivity of syngas conversion on ZnO surfaces with complex reaction network and structural evolution. *ACS Catal.* **11**, 12264–12273 (2021).
24. He, Z., Li, X. B., Liu, L. M. & Zhu, W. The intrinsic mechanism of methane oxidation under explosion condition: a combined ReaxFF and DFT study. *Fuel* **124**, 85–90 (2014).
25. Hannagan, R. T. et al. First-principles design of a single-atom—alloy propane dehydrogenation catalyst. *Science* **372**, 1444–1447 (2021).
26. Ulissi, Z. W., Medford, A. J., Bligaard, T. & Nørskov, J. K. To address surface reaction network complexity using scaling relations machine learning and DFT calculations. *Nat. Commun.* **8**, 1–7 (2017).
27. Latimer, A. A. et al. Understanding trends in C-H bond activation in heterogeneous catalysis. *Nat. Mater.* **16**, 225–229 (2017).
28. Schweitzer, J.-M. et al. Multiscale modeling as a tool for the prediction of catalytic performances: the case of n-heptane hydroconversion in a large-pore zeolite. *ACS Catal.* **12**, 1068–1081 (2022).
29. Bruix, A., Margraf, J. T., Andersen, M. & Reuter, K. First-principles-based multiscale modelling of heterogeneous catalysis. *Nat. Catal.* **2**, 659–670 (2019).
30. Ohno, K. & Maeda, S. Global reaction route mapping on potential energy surfaces of formaldehyde, formic acid, and their metal-substituted analogues. *J. Phys. Chem. A* **110**, 8933–8941 (2006).
31. Maeda, S., Ohno, K. & Morokuma, K. Systematic exploration of the mechanism of chemical reactions: the global reaction route mapping (GRRM) strategy using the ADDF and AFIR methods. *Phys. Chem. Chem. Phys.* **15**, 3683–3701 (2013).
32. Maeda, S., Komagawa, S., Uchiyama, M. & Morokuma, K. Finding reaction pathways for multicomponent reactions: the passerini reaction is a four-component reaction. *Angew. Chem. - Int. Ed.* **50**, 644–649 (2011).
33. Maeda, S., Taketsugu, T., Ohno, K. & Morokuma, K. From roaming atoms to hopping surfaces: mapping out global reaction routes in photochemistry. *J. Am. Chem. Soc.* **137**, 3433–3445 (2015).
34. Maeda, S., Harabuchi, Y., Ono, Y., Taketsugu, T. & Morokuma, K. Intrinsic reaction coordinate: calculation, bifurcation, and automated search. *Int J. Quantum Chem.* **115**, 258–269 (2015).
35. Maeda, S., Sugiyama, K., Sumiya, Y., Takagi, M. & Saita, K. Global reaction route mapping for surface adsorbed molecules: a case study for H2O on Cu(111) surface. *Chem. Lett.* **47**, 396–399 (2018).
36. Sugiyama, K., Sumiya, Y., Takagi, M., Saita, K. & Maeda, S. Understanding CO oxidation on the Pt(111) surface based on a reaction route network. *Phys. Chem. Chem. Phys.* **21**, 14366–14375 (2019).
37. Yoshimura, T. et al. Exploring the full catalytic cycle of rhodium(i)-BINAP-catalysed isomerisation of allylic amines: a graph theory approach for path optimisation. *Chem. Sci.* **8**, 4475–4488 (2017).
38. Maeda, S. et al. Implementation and performance of the artificial force induced reaction method in the GRRM17 program. *J. Comput. Chem.* **39**, 233–250 (2018).
39. Hayashi, H. et al. Synthesis of difluoroglycine derivatives from amines, difluorocarbene, and CO_2: computational design, scope, and applications. *Chem. Eur. J.* **27**, 1–9 (2021).
40. Mita, T., Harabuchi, Y. & Maeda, S. Discovery of a synthesis method for a difluoroglycine derivative based on a path generated by quantum chemical calculations. *Chem. Sci.* **11**, 7569–7577 (2020).
41. Sugiyama, K., Saita, K. & Maeda, S. A reaction route network for methanol decomposition on a Pt(111) surface. *J. Comput. Chem.* **42**, 2163–2169 (2021).
42. Oyama, S. T. Chemical and catalytic properties of ozone. *Catal. Rev. Sci. Eng.* **42**, 279–322 (2000).
43. Sugasawa, M. & Ogata, A. Effect of different combinations of metal and zeolite on ozone-assisted catalysis for toluene removal. *Ozone Sci. Eng.* **33**, 158–163 (2011).
44. Kim, H. H. et al. Ozone-assisted catalysis of toluene with layered ZSM-5 and Ag/ZSM-5 zeolites. *Plasma Chem. Plasma Process.* **33**, 1083–1098 (2013).
45. Chao, C. Y. H., Kwong, C. W. & Hui, K. S. Potential use of a combined ozone and zeolite system for gaseous toluene elimination. *J. Hazard. Mater.* **143**, 118–127 (2007).
46. Xi, Y., Reed, C., Lee, Y. K. & Oyama, S. T. Acetone oxidation using ozone on manganese oxide catalysts. *J. Phys. Chem. B* **109**, 17587–17596 (2005).
47. Reed, C., Xi, Y. & Oyama, S. T. Distinguishing between reaction intermediates and spectators: a kinetic study of acetone oxidation using ozone on a silica-supported manganese oxide catalyst. *J. Catal.* **235**, 378–392 (2005).
48. Einaga, H. & Futamura, S. Catalytic oxidation of benzene with ozone over alumina-supported manganese oxides. *J. Catal.* **227**, 304–312 (2004).
49. Einaga, H., Maeda, N. & Teraoka, Y. Effect of catalyst composition and preparation conditions on catalytic properties of unsupported manganese oxides for benzene oxidation with ozone. *Appl. Catal. B* **142–143**, 406–413 (2013).
50. Božović, A. et al. Conversion of methane to methanol: Nickel, palladium, and platinum (d 9) cations as catalysts for the oxidation of methane by ozone at room temperature. *Chem. Eur. J.* **16**, 11605–11610 (2010).
51. McDonald, D. C. et al. Temperature and isotope dependent kinetics of nickel-catalyzed oxidation of methane by ozone. *J. Phys. Chem. A* **122**, 6655–6662 (2018).
52. Dillemuth, F. J., Skidmore, D. R. & Schubert, C. C. The reaction of ozone with methane. *J. Phys. Chem.* **64**, 1496–1499 (1960).

53. Hui, K. S., Kwong, C. W. & Chao, C. Y. H. Methane emission abatement by Pd-ion-exchanged zeolite 13X with ozone. *Energy Environ. Sci.* **3**, 1092–1098 (2010).
54. Keenan, M., Nicole, J. & Poojary, D. Ozone as an enabler for low temperature methane control over a current production Fe-BEA catalyst. *Top. Catal.* **62**, 351–355 (2019).
55. Jin, S. M., Lee, K. Y. & Lee, D. W. Ozone-induced lean methane oxidation over cobalt ion-exchanged BEA catalyst under dry reaction conditions. *J. Ind. Eng. Chem.* **112**, 296–306 (2022).
56. Ito, Y. Methane purification method and methance purification system. JPA P2017-170309A (2017).
57. Wan, M. P., Hui, K. S., Chao, C. Y. H. & Kwong, C. W. Catalytic combustion of methane with ozone using Pd-exchanged zeolite X: experimental investigation and kinetics model. *Combust. Sci. Technol.* **182**, 1429–1445 (2010).
58. Mahyuddin, M. H., Shiota, Y., Staykov, A. & Yoshizawa, K. Theoretical investigation of methane hydroxylation over isoelectronic [FeO]2+- and [MnO]+-exchanged zeolites activated by N_2O. *Inorg. Chem.* **56**, 10370–10380 (2017).
59. Gannouni, A., Michel, C., Delbecq, F., Zina, M. S. & Sautet, P. DFT investigations for the catalytic reaction mechanism of methane combustion occurring on Pd(ii)/Al-MCM-41. *Phys. Chem. Chem. Phys.* **20**, 25377–25386 (2018).
60. Liu, C., Tranca, I., van Santen, R. A., Hensen, E. J. M. & Pidko, E. A. Scaling relations for acidity and reactivity of zeolites. *J. Phys. Chem. C.* **121**, 23520–23530 (2017).
61. Sandoval-Díaz, L. E., González-Amaya, J. A. & Trujillo, C. A. General aspects of zeolite acidity characterization. *Microporous Mesoporous Mater.* **215**, 229–243 (2015).
62. Farneth, W. E. & Gorte, R. J. Methods for characterizing zeolite acidity. *Chem. Rev.* **95**, 615–635 (1995).
63. Boronat, M. & Corma, A. What is measured when measuring acidity in zeolites with probe molecules? *ACS Catal.* **9**, 1539–1548 (2019).
64. Grifoni, E. et al. Confinement effects and acid strength in zeolites. *Nat. Commun.* **12**, 2630 (2021).
65. Perdew, J. P., Burke, K. & Ernzerhof, M. Generalized gradient approximation made simple. *Phys. Rev. Lett.* **77**, 3865–3868 (1996).
66. Kresse, G. & Hafner, J. Ab initio molecular dynamics for open-shell transition metals. *Phys. Rev. B* **48**, 13115–13118 (1993).
67. Kresse, G. & Hafner, J. Ab initio molecular-dynamics simulation of the liquid-metal–amorphous-semiconductor transition in germanium. *Phys. Rev. B* **49**, 14251–14269 (1994).
68. Blöchl, P. E. Projector augmented-wave method. *Phys. Rev. B* **50**, 17953–17979 (1994).
69. Kresse, G., Joubert, D., Kresse, G. & Joubert, D. From ultrasoft pseudopotentials to the projector augmented-wave method. *Phys. Rev. B* **59**, 1758–1775 (1999).
70. Monkhorst, H. J. & Pack, J. D. Special points for Brillouin-zone integrations. *Phys. Rev. B* **13**, 5188–5192 (1976).
71. Grimme, S., Ehrlich, S. & Goerigk, L. Effect of the damping function in dispersion corrected density functional theory. *J. Comput Chem.* **32**, 1456–1465 (2011).
72. Baerlocher, C., McCusker, L.B., van Koningsveld, H. Database of zeolite structures; http://www.iza-structure.org/databases/ (accessed Jun 2021).
73. Fukui, K. The path of chemical reactions—the IRC Approach. *Acc. Chem. Res.* **14**, 363 (1981).
74. Dronskowski, R. & Blochl, P. E. Crystal orbital hamilton populations (COHP). Energy-resolved visualization of chemical bonding in solids based on density-functional calculations. *J. Phys. Chem.* **97**, 8617–8624 (1993).
75. Maintz, S., Deringer, V. L., Tchougréeff, A. L. & Dronskowski, R. LOBSTER: a tool to extract chemical bonding from plane-wave based DFT. *J. Comput. Chem.* **37**, 1030–1035 (2016).
76. Wang, Y. VASPMO, version 0.41., 2021.
77. Momma, K. & Izumi, F. VESTA 3 for three-dimensional visualization of crystal, volumetric and morphology data. *J. Appl. Crystallogr.* **44**, 1272–1276 (2011).
78. Vandevondele, J. et al. Quickstep: Fast and accurate density functional calculations using a mixed Gaussian and plane waves approach. *Comput. Phys. Commun.* **167**, 103–128 (2005).
79. VandeVondele, J. & Hutter, J. Gaussian basis sets for accurate calculations on molecular systems in gas and condensed phases. *J. Chem. Phys.* **127**, 114105 (2007).
80. Goedecker, S. & Teter, M. Separable dual-space Gaussian pseudopotentials. *Phys. Rev. B Condens. Matter Mater. Phys.* **54**, 1703–1710 (1996).
81. Hartwigsen, C., Goedecker, S. & Hutter, J. Relativistic separable dual-space Gaussian pseudopotentials from H to Rn. *Phys. Rev. B* **58**, 3641–3662 (1998).

Acknowledgements

This research was financially supported by JST-CREST (JPMJCR17J3) and JSPS KAKENHI (21H04626) grants. Some of the calculations were conducted employing the supercomputing resources at the Cyberscience Center of Tohoku University. This research was also supported by the Joint Usage/Research Center for Catalysis. S.Y. is grateful to the MANABIYA system of the Institute for Chemical Reaction Design and Discovery (ICReDD) of Hokkaido University, which was established by the World Premier International Research Initiative (WPI), MEXT, Japan, to support the learning of the GRRM program techniques for DFT calculations. This research is one of the projects promoted by the Research Association of Automotive Internal Combustion Engines (AICE) and is financially supported by the Japan Ministry of Economy, Trade, and Industry. The authors acknowledge the Technical Division of the Institute for Catalysis of Hokkaido University. S.Y. acknowledges the Grant-in-Aid for JSPS Fellows (21J11744, DC2).

Author contributions

S.Y. wore the draft and carried out DFT calculations as well as the most of experiments. K.Sa. and T.Ta. deeply discussed the applied computational approach and critically supported for utilization of GRRM program. T.M. and K.N. conducted the kinetic analysis for CH_4 combustion reaction. K.K. prepared the catalysts and performed NH3 adsorption measurements. K.Sa, T.Ta, T.To., and Z.M. critically revised the manuscript. K.Sh. designed and supervised the whole project.

Competing interests

The authors declare no competing interests.

Additional information

Supplementary information The online version contains supplementary material available at https://doi.org/10.1038/s41467-023-39541-y.

Correspondence and requests for materials should be addressed to Ken-ichi Shimizu.

Peer review information *Nature Communications* thanks Qi An and the other, anonymous, reviewers for their contribution to the peer review of this work.